

Ledge-flow-controlled catalyst interface dynamics during Si nanowire growth

STEPHAN HOFMANN^{1*}, RENU SHARMA², CHRISTOPH T. WIRTH¹, FELIPE CERVANTES-SODI¹, CATERINA DUCATI³, TAKESHI KASAMA³, RAFAL E. DUNIN-BORKOWSKI⁴, JEFF DRUCKER⁵, PETER BENNETT⁵ AND JOHN ROBERTSON¹

¹Department of Engineering, University of Cambridge, Cambridge CB3 0FA, UK

²LeRoy Eyring Center for Solid State Science, Arizona State University, Tempe, Arizona 85287-1704, USA

³Department of Materials Science and Metallurgy, University of Cambridge, Cambridge CB2 3QZ, UK

⁴Center for Electron Nanoscopy, Technical University of Denmark, DK-2800 Kongens Lyngby, Denmark

⁵Department of Physics, Arizona State University, Tempe, Arizona 85287-1504, USA

*e-mail: sh315@cam.ac.uk

Published online: 9 March 2008; doi:10.1038/nmat2140

Self-assembled nanowires offer the prospect of accurate and scalable device engineering at an atomistic scale for applications in electronics, photonics and biology. However, deterministic nanowire growth and the control of dopant profiles and heterostructures are limited by an incomplete understanding of their interface dynamics^{1,2}. Although catalytic chemical vapour deposition of nanowires below the eutectic temperature has been demonstrated in many semiconductor–catalyst systems^{3–6}, growth from solid catalysts is still disputed and the overall mechanism is largely unresolved. Here, we present a video-rate environmental transmission electron microscopy study of Si nanowire formation from Pd silicide crystals under disilane exposure. A Si crystal nucleus forms by phase separation, as observed for the liquid Au–Si system, which we use as a comparative benchmark. The dominant coherent Pd silicide/Si growth interface subsequently advances by lateral propagation of ledges, driven by catalytic dissociation of disilane and coupled Pd and Si diffusion. Our results establish an atomistic framework for nanowire assembly from solid catalysts, relevant also to their contact formation.

The catalytic chemical vapour deposition (CVD) of nanowires occurs by several sequential processes: (1) gas precursor transport, (2) precursor adsorption and dissociation at the catalyst surface, (3) material diffusion across the catalyst particle and (4) precipitation of nanowire material. The often cited vapour–liquid–solid (VLS) mechanism refers to catalyst liquefaction during nanowire CVD, typically by alloying with the substrate or during steps (2) and (3) (ref. 1). High-aspect-ratio nanowires are formed because of a higher reactive sticking probability of the gas on the catalyst surface and precipitation at the catalyst–nanowire interface¹. Nevertheless, the present atomic-level understanding of nanowire growth is incomplete, in particular for technologically relevant nanometre-sized catalysts. Post-growth analyses lead to contradictory explanations as to the state of the catalyst, the role of melting point depression and the rate-limiting step^{3–5,7,8}. *In situ* electron microscopy for the Au–Ge system has shown that the state of the catalyst alloy can be either liquid or solid, and that a large undercooling relative to the bulk eutectic can occur owing to Ge

supersaturation⁶. However, for either a VLS or a vapour–solid–solid (VSS) framework, there has been no discussion of the catalyst interface dynamics and the initial phases of nanowire formation. It is known that, in general, interfacial roughening determines the crystal growth mode^{9,10}. Atomic steps are also known to play a central role in heterogeneous nucleation and interface propagation for thin films and nanostructures such as quantum dots¹¹.

Here, we expose pre-evaporated Pd and Au films on silicon oxide (SiO_x) membranes to disilane in an environmental transmission electron microscope (ETEM). This provides a lattice-resolved, video-rate record of all stages of Si nanowire (SiNW) growth under realistic conditions used in standard CVD reactors. Figure 1a,d shows Au and Pd catalyst crystals on SiO_x. Introducing Si₂H₆ causes Au particles to show contrast fluctuations, swell and liquefy as Si is incorporated (Fig. 1b), whereas Pd forms solid silicide crystals (Fig. 1e,f). The Au–Si bulk phase diagram has a simple eutectic at $T_c = 363^\circ\text{C}$, with a mutual insolubility of the elements in the solid, and no stable compounds. The Au-rich alloy has a close-packed structure up to 40 at% Si (ref. 12). As Si has a lower surface free energy than Au, the liquid Au–Si alloy surface will be Si rich¹³. Melting causes the particles to change from a polyhedral to a circular cross-section as the surface free energies become isotropic.

In contrast, the bulk Pd–Si binary phase diagram has many stable, Pd-rich silicides and a minimum eutectic temperature of 810°C (ref. 14). On the Si-rich side, PdSi decomposes below 824°C in a eutectoid reaction to give Pd₂Si and Si (ref. 14). From the TEM projected images, we extrapolate a truncated polyhedral Pd crystal ~ 5.9 nm across to expand by ~ 40 vol% after exposure to disilane at 670°C , which is consistent with conversion to crystalline Pd₂Si. We recorded the process in ~ 0.4 s, which suggests a diffusion coefficient of Si through crystalline Pd of over $\sim 1 \times 10^{-17} \text{ m}^2 \text{ s}^{-1}$ and converts into an average Si incorporation rate of the order of $\sim 3,000 \text{ atoms s}^{-1}$ or a rate of $\sim 30 \text{ Si atoms s}^{-1}$ per square nanometre of crystal surface area. This allows us to estimate a reactive sticking probability S for disilane of $\sim 10^{-3}$, which compares (within the error of our approximations) to $S \sim 10^{-2}$ for liquid Au–Si under conditions used to record Fig. 1b. Post-growth selected-area diffraction of the catalyst particles also shows

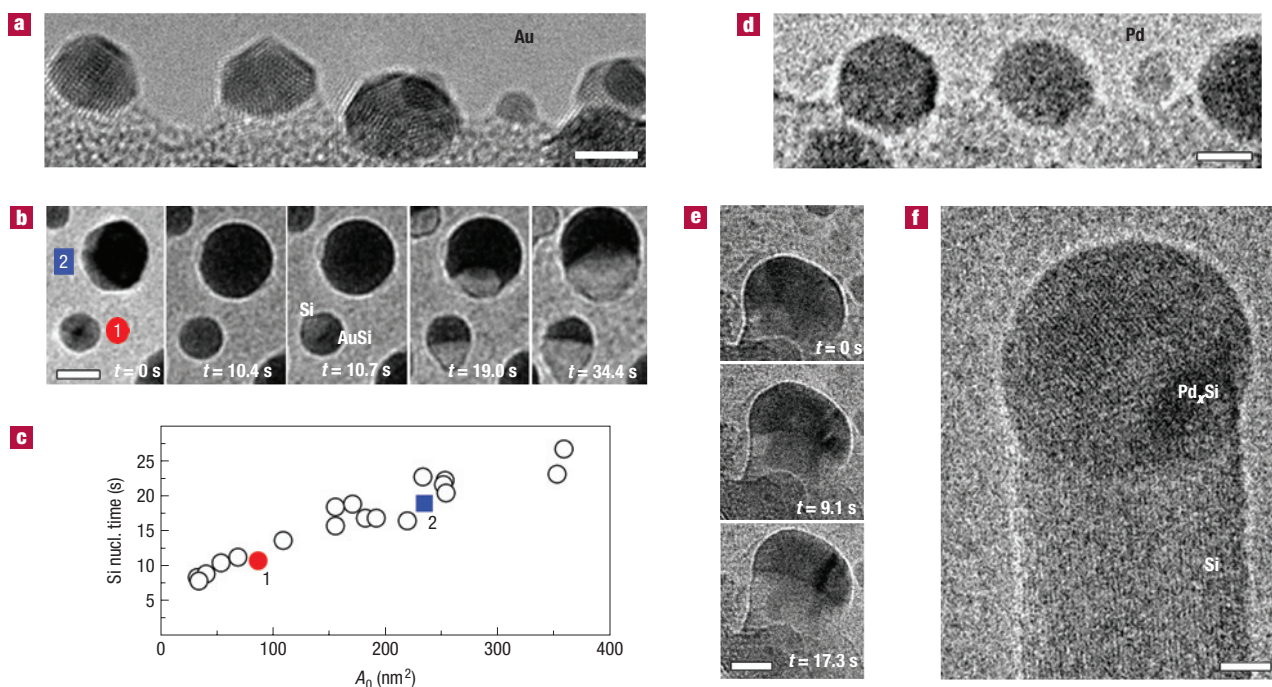


Figure 1 SiNW nucleation from liquid and solid catalysts. **a**, As-evaporated ~ 1 nm Au on SiO_x (scale bar 3 nm). **b**, Plan-view ETEM image sequence of Au– SiO_x system exposed to $\sim 1.3 \times 10^{-4}$ mbar Si_2H_6 at 590°C (scale bar 10 nm, Supplementary Information, video S1). $t = 0$ s roughly reflects the onset of disilane exposure. **c**, Incubation time for Si precipitation versus A_0 , the cross-sectional area of the initial Au crystal (data from Supplementary Information, video S1). The Au–Si islands labelled in **b** are indicated. **d**, 0.5 nm Pd on SiO_x at 670°C in vacuum ($\sim 10^{-6}$ mbar, scale bar 3 nm). **e**, ETEM image sequence of Pd– SiO_x system exposed to $\sim 1.6 \times 10^{-2}$ mbar Si_2H_6 at $\sim 750^\circ\text{C}$ (scale bar 10 nm). t indicates elapsed time with respect to the first image. **f**, ETEM image of tip region of Pd-silicide-catalysed SiNW at $\sim 715^\circ\text{C}$ during disilane exposure as in **e** (scale bar 3 nm, Supplementary Information, video S2). The SiNW growth direction is $\langle 112 \rangle$.

the presence of Pd_2Si . The silicide crystals show high deformability during nanowire formation, analogous to Ni crystals during carbon nanotube nucleation and growth¹⁵.

The SiNW formation dynamics for the different catalyst systems show clear similarities. Figure 1b and Supplementary Information, video S1 show that Si nucleation occurs burst-like, by growing into the Au–Si droplet. We find that smaller catalyst particles nucleate Si first (Fig. 1c). The rate of Si inclusion scales with catalyst surface area, that is, \sim radius R^2 for spherical catalyst particles, whereas the Si concentration is $\sim R^{-3}$. Hence, the Si concentration reaches the supersaturation threshold at a rate $\sim 1/R$ and Si nucleation time $\sim R_0 \sim \sqrt{A_0}$, where A_0 is the cross-sectional area of the initial Au crystal (Fig. 1c). The liquid–solid interfaces advance outwards resulting in the Au–Si alloy droplet eventually sitting on a Si crystal with a wetting angle of $\sim 120^\circ$ (Fig. 1c, Supplementary Information, video S1). Si(111) is the slowest growing face with the lowest free energy and thus dominates SiNW growth^{1,16}. Secondary nucleation is suppressed, so each catalyst particle normally has only one growth front. The catalyst droplets undergo significant reshaping owing to their high density and coalescence (Fig. 1c, Supplementary Information, video S1). This creates an intermediate stage where larger catalyst droplets have several growth fronts. We observe an Ostwald ripening-like process, driven by interfacial energy minimization, whereby crystalline Si dissolves back into the Au–Si droplet and diffuses to a larger (~ 20 – 30 nm) liquid–solid interface, eventually reabsorbing all growth fronts except one. These processes constitute SiNW tip growth.

Pd-silicide-mediated Si crystal formation is shown in Fig. 1e,f. The Si nuclei grow by movement of coherent, semi-coherent facets

and smoothly curved incoherent interfaces. Pd_2Si crystallizes in a hexagonal structure (space group $P62m$) and its close-packed (0001) plane is found to be coherent to the close-packed Si(111) plane (with $[11\bar{2}]\parallel[2\bar{1}\bar{1}0]$ mismatch $\sim 1.8\%$) (ref. 17) with the resulting interface atomically abrupt to ~ 0.3 nm (ref. 18). The rough, incoherent interfaces move faster and vanish, leaving the smooth, coherent interfaces to limit the overall growth rate. The Pd silicide/SiNW interface is generally very dynamic, constantly fluctuating, forming and annihilating facets as it propagates (see Supplementary Information, videos S2,S3). By analogy to the Au–Si system, one Si growth front opens for each catalyst particle, which eventually pushes the Pd silicide crystal into the tip of the newly formed SiNW, Fig. 1f. The coalescence of particles/nanowires, however, can temporarily lead to multiple Si growth fronts.

SiNW growth requires some form of material transport across the catalyst. Whereas the Si solubility and diffusivity in the liquid Au–Si droplet are high and the rate-limiting step is the catalytic dissociation of disilane¹⁹, the mechanism for step (3) in the Pd–Si system is less obvious. We determine Pd-silicide-catalysed SiNW growth rates to be over 5 nm s^{-1} for 20–60-nm-diameter SiNWs at 620–670 °C and 1.2 – 1.6×10^{-2} mbar Si_2H_6 (Fig. 2). SiNW growth ceased below $\sim 520^\circ\text{C}$. The growth process can be compared to Pd_2Si -mediated Si film crystallization, where the silicide acts as a transport layer mediating Si and Pd diffusion^{20,21}. The reported recrystallization rate is $\sim 100 \mu\text{m}$ per 10 h, that is, 2.8 nm s^{-1} , at 500°C (ref. 22). This is more than 10 times faster than SiNW growth rates observed at 560°C ; thus, diffusion or reactions at the Pd silicide/SiNW interface are clearly not rate limiting. Owing to a Pilling–Bedworth ratio close to 2, the coupling of Si and Pd diffusion fluxes has been suggested to avoid stress build-up²¹. This

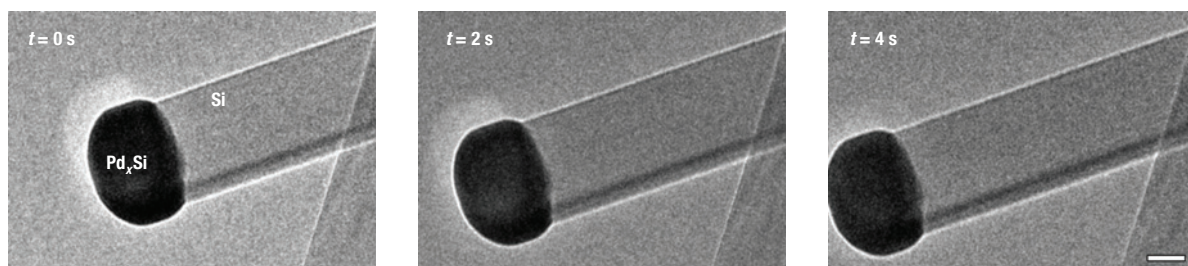


Figure 2 Pd-silicide-mediated nanowire growth rate. ETEM image sequence of SiNW tip region at $\sim 625^\circ\text{C}$ during exposure to $\sim 1.3 \times 10^{-2}$ mbar Si_2H_6 (scale bar 20 nm). t indicates elapsed time with respect to the first image.

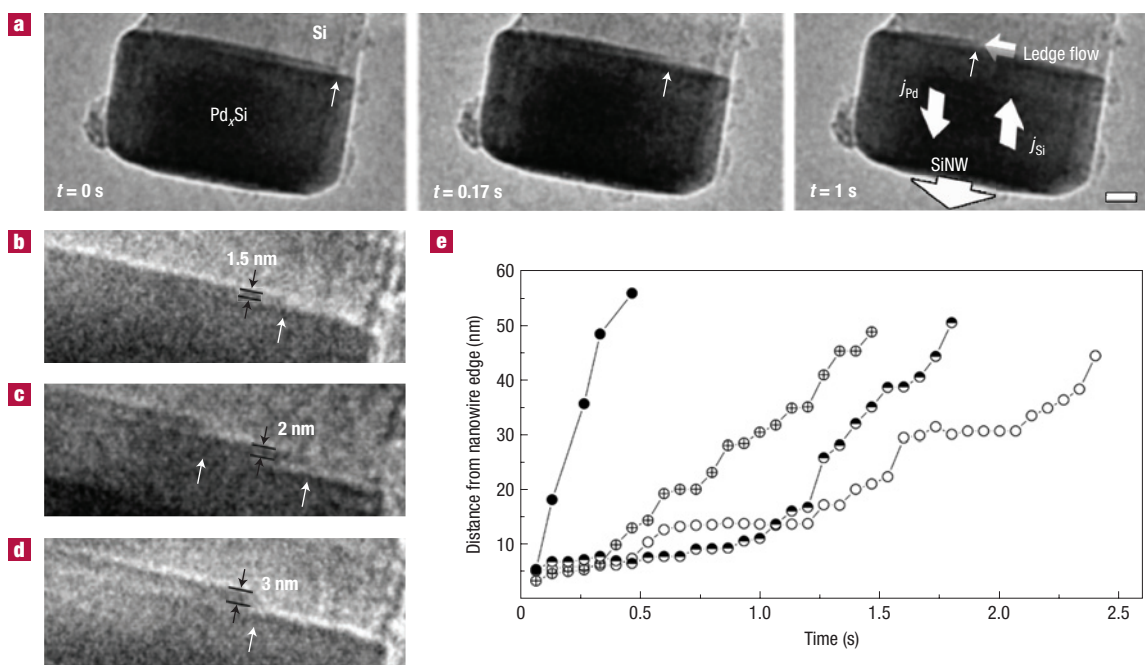


Figure 3 Ledge-flow-controlled catalyst interface dynamics. **a**, ETEM image sequence of growing SiNW at $\sim 560^\circ\text{C}$ in $\sim 1.2 \times 10^{-2}$ mbar Si_2H_6 (scale bar 10 nm). t indicates elapsed time with respect to the first image. The ledge flow, growth direction and diffusion fluxes are shown schematically. **b–d**, Various ledge configurations at the Pd silicide/SiNW interface during disilane exposure. **e**, Measured step edge position versus time for four independent ledges of roughly equal ~ 1.7 nm height in projection.

predicts a flux ratio $j_{\text{Si}}/j_{\text{Pd}}$ around 0.5. Hence, we propose that SiNWs grow by the diffusion of Pd away from the silicide/SiNW interface across the silicide particle to the top surface, coupled to a smaller Si flux in the opposite direction. Pd solubility in crystalline Si is low. Thus, Pd is continuously expelled from the growing SiNW.

The continued SiNW growth and propagation of the catalyst–Si interface depends on interfacial roughness. Figure 3a shows a sequence of frames extracted from an ETEM video of Pd-silicide-catalysed SiNW growth at $\sim 560^\circ\text{C}$ in $\sim 1.2 \times 10^{-2}$ mbar Si_2H_6 . The catalyst silicide/SiNW interface is flat in projection, which indicates that a (semi)coherent interface limits growth. We observe the lateral propagation of ledges. The step height varies, but can be as much as ~ 3 nm, or ~ 10 {111}Si lattice spacings. Although ledge and superledge propagation have been observed before, for example, for NiSi_2/Si thin-film solid-state reactions²³ and for $\gamma\text{-Ag}_2\text{Al}$ precipitate plates in an

Al–Ag alloy⁹, the details of interface propagation have, to our knowledge, never been considered in the framework of a VSS model for nanowire growth. During continuous exposure to Si_2H_6 , the rate of step formation can be as low as 1 per 5 s (see Supplementary Information, video S4). New ledges can be generated by various mechanisms, such as repeated surface nucleation, spiral growth, nucleation at precipitate edges or from intersections with other precipitates⁹. We observe step nucleation as repetitive but independent events; hence, we can exclude a growth mechanism based on one screw dislocation²⁴. Ledge flow begins at the edges of the nanowire and can be in either direction across the SiNW interface. This is consistent with their nucleation at the nanowire surface. The measured step heights refer to the recorded TEM projection, and hence are snapshots varying with nanowire orientation and direction of step flow. Figure 3e shows the distance of ~ 1.7 -nm-high step edges to the nanowire edge

over time. We observe frequent slowing and halting, presumably at interface defects. The maximum ledge velocity is $\sim 130 \text{ nm s}^{-1}$ in Fig. 3e. Averaging over the halting lets us estimate lower average ledge velocities of $\sim 25 \text{ nm s}^{-1}$. Within a 0.7–3 nm step height range, we observe that higher steps tend to halt more often, and hence have lower average ledge velocities. The maximum ledge velocity, however, does not seem to scale with step height. Thus, our data suggest a nucleation-limited regime, but a larger data set is required to comment in more detail, in particular on the relation of nucleation frequency to ledge height and the influence of strain fields and chemical gradients.

Multiple steps (Fig. 3c) propagating in the same direction can merge and form larger steps. We find that the axial net growth of the SiNW is roughly equal to the average volume change estimated by integrating the ledge flow. This confirms that in Fig. 3 all growth occurs via lateral ledge flow, rather than including continuous growth on atomically rough, incoherent interfaces. The intermittent start of new steps suggests that the step flow is inhibited by a nucleation event. Interface steps intrinsically contain a dislocation¹⁷, and a lattice mismatch eases the strain of the dislocation core, perhaps contributing to the low-temperature mobility.

Our model for Pd-catalysed SiNW growth is shown schematically in Fig. 3a: Pd leaves the $\text{Pd}_x\text{Si}/\text{c-Si}$ interface, diffuses through or around the Pd_xSi particle and reacts at its free surface with the excess Si, generated by decomposition of disilane there. Stress build-up at the SiNW–catalyst interface is prevented by Si diffusion in the other direction. The driving force is the Si concentration gradient and, as in the Au–Si system, gas decomposition on the catalyst surface is the rate-limiting step, under our growth conditions. Our model implies that the diffusing species during SiNW growth, collectively referred to as step (3), depend on the choice of catalyst and its relevant silicide. Under similar growth conditions, metal diffusion away from the nanowire interface will dominate for catalysts such as Ni, whereas Si diffusion towards the nanowire interface will dominate for catalysts such as Ti and Fe (ref. 25). We note that this diffusion behaviour can also be seen during the formation of electrical contacts to SiNWs, for example, for Ni (ref. 26).

To conclude, we presented lattice-resolved ETEM recordings of SiNW nucleation and growth from Pd silicide catalyst crystals and liquid Au–Si alloy droplets. The catalyst–Si interface free energies are lowest for atomically flat, coherent close-packed planes, for example, $\text{Pd}_2\text{Si}(0001)/\text{Si}(111)$. These interfaces advance via the lateral propagation of ledges, which is a slower process than continuous growth of rough, incoherent interfaces. We directly resolved such ledge flow for Pd-silicide-mediated SiNW growth. We propose that growth by ledges is an important part of a VSS growth mechanism. Ledge flow can also be expected for a VLS mechanism, but further studies on kinetic roughening of solid–liquid interfaces^{10,27} during nanowire growth are needed to confirm this.

METHODS

We used a modified Tecnai F20 ETEM, operated at 200 kV, equipped with a differential pumping system and a Gatan imaging filter²⁸. The microscope permits pressures of up to 10 mbar, with a specified information limit of 0.14 nm. Digital video sequences can be recorded with 15 frames s^{-1} time resolution. Given temperatures refer to thermocouple readings on the TEM holder mini-furnace. The electron dose was representative of that typically

implemented for high-resolution imaging²⁹, and the electron beam was never focused onto the specimen to minimize the effects of electron-beam-induced damage and modification of the specimen. Thin Au, Pd films ($< 1 \text{ nm}$, 99.9% purity) were thermally evaporated (base pressure $\sim 10^{-6}$ mbar, substrates at approximately room temperature) onto perforated SiO_x membranes (SPI supplies), 400 mesh Ni TEM grids coated with a SiO_x membrane or onto 2000 mesh Cu TEM grids coated with a holey carbon film (Agar Scientific) and a $\sim 30 \text{ nm}$ sputtered SiO_x layer. The samples were transferred in air to the ETEM. Sub-2-nm-thick Au readily formed nanometre-sized islands as-evaporated on SiO_x . Solid-state dewetting of semicontinuous nominally 1-nm-thick Pd defined islands with a size distribution centred around 5–10 nm on annealing in vacuum ($< 10^{-6}$ mbar) to growth temperatures between 350 and 810 °C. Coarsening increased their average size for prolonged heating. At high temperatures, silicidation could also be observed due to SiO_2 reduction. Undiluted disilane in a pressure range of 10^{-4} –0.1 mbar was used for ETEM chemical vapour deposition.

Received 25 October 2007; accepted 7 February 2008; published 9 March 2008.

References

- Wagner, R. S. in *Whisker Technology* (ed. Levitt, A. P.) (Wiley, New York, 1970).
- Hiruma, K. *et al.* Growth and optical properties of nanometer-scale GaAs and InAs whiskers. *J. Appl. Phys.* **77**, 447–462 (1995).
- Kamins, T. I., Williams, R. S., Basile, D. P., Hesjedal, T. & Harris, J. S. Ti-catalyzed Si nanowires by chemical vapor deposition: Microscopy and growth mechanisms. *J. Appl. Phys.* **89**, 1008–1016 (2001).
- Persson, A. I. *et al.* Solid-phase diffusion mechanism for GaAs nanowire growth. *Nature Mater.* **3**, 677–681 (2004).
- Wang, Y. W., Schmidt, V., Senz, S. & Gosele, U. Epitaxial growth of silicon nanowires using an aluminium catalyst. *Nature Nanotechnol.* **1**, 186–189 (2006).
- Kodambaka, S., Tersoff, J., Reuter, M. C. & Ross, F. M. Germanium nanowire growth below the eutectic temperature. *Science* **316**, 729–732 (2007).
- Park, H. D., Gaillot, A.-C., Prokes, S. M. & Cammarata, R. C. Observation of size dependent liquidus depression in the growth of InAs nanowires. *J. Cryst. Growth* **296**, 159–164 (2006).
- Adhikari, H., Marshall, A. F., Chidsey, C. E. D. & McIntyre, P. C. Germanium nanowire epitaxy: Shape and orientation control. *Nano Lett.* **6**, 318–323 (2006).
- Howe, J. M. *Interfaces in Materials* (Wiley, New York, 1997).
- Jackson, K. A. The present state of the theory of crystal growth from the melt. *J. Cryst. Growth* **24–25**, 130–136 (1974).
- Hannon, J. B., Shenoy, V. B. & Schwarz, K. W. Anomalous spiral motion of steps near dislocations on silicon surfaces. *Science* **313**, 1266–1269 (2006).
- Mangin, P., Marchal, G., Mourey, C. & Janot, C. Physical studies of $\text{Au}(x)\text{Si}(1-x)$ amorphous alloys. *Phys. Rev. B* **21**, 3047–3056 (1980).
- Shpyrko, O. G. *et al.* Surface crystallization in a liquid AuSi alloy. *Science* **313**, 77–80 (2006).
- Baxi, H. C. & Massalski, T. B. The Pd–Si System. *J. Phase Equilib.* **12**, 349–356 (1991).
- Hofmann, S. *et al.* In situ observations of catalyst dynamics during surface-bound carbon nanotube nucleation. *Nano Lett.* **7**, 602–608 (2007).
- Wu, Y. *et al.* Controlled growth and structures of molecular-scale silicon nanowires. *Nano Lett.* **4**, 433–436 (2004).
- Cherns, D., Smith, D. A., Krakow, W. & Batson, P. E. Electron-microscope studies of the structure and propagation of the $\text{Pd}_2\text{Si}(111)/\text{Si}$ interface. *Phil. Mag.* **A 45**, 107–125 (1982).
- Rubloff, G. W. Microscopic properties and behavior of silicide interfaces. *Surf. Sci.* **132**, 268–314 (1983).
- Kodambaka, S., Tersoff, J., Reuter, M. C. & Ross, F. M. Diameter-independent kinetics in the vapor–liquid–solid growth of Si nanowires. *Phys. Rev. Lett.* **96**, 096105 (2006).
- Liau, Z. L., Campisano, S. U., Canali, C., Lau, S. S. & Mayer, J. W. Kinetics of the initial stage of Si transport through Pd-silicide for epitaxial growth. *J. Electrochem. Soc.* **122**, 1696–1699 (1975).
- Goessele, U. in *Alloying* (eds Walter, J. L., Jackson, M. R. & Sims, C. T.) (ASM, Ohio, 1988).
- Lee, S. W., Jeon, Y. C. & Joo, S. K. Pd induced lateral crystallization of amorphous Si thin-films. *Appl. Phys. Lett.* **66**, 1671–1673 (1995).
- Hesse, D., Werner, P., Mattheis, R. & Heydenreich, J. Interfacial reaction barriers during thin-film solid-state reactions—the crystallographic origin of kinetic barriers at the $\text{NiSi}_2/\text{Si}(111)$ interface. *Appl. Phys.* **A 57**, 415–425 (1993).
- Frank, F. C. The influence of dislocations on crystal growth. *Discuss. Faraday Soc.* **5**, 48–54 (1949).
- Landolt-Bornstein (ed.) *Diffusion in Semiconductors III/33* (Springer, Berlin, 1998).
- Weber, W. M. *et al.* Silicon-nanowire transistors with intruded nickel-silicide contacts. *Nano Lett.* **6**, 2660–2666 (2006).
- Saka, H., Sasaki, K., Tsukimoto, S. & Arai, S. In situ observation of solid–liquid interfaces by transmission electron microscopy. *J. Mater. Res.* **20**, 1629–1640 (2005).
- Sharma, R. An environmental transmission electron microscope for in situ synthesis and characterization of nanomaterials. *J. Mater. Res.* **20**, 1695–1707 (2005).
- Yokota, T., Murayama, M. & Howe, J. M. In situ transmission-electron-microscopy investigation of melting in submicron Al–Si alloy particles under electron-beam irradiation. *Phys. Rev. Lett.* **91**, 265504 (2003).

Acknowledgements

S.H. acknowledges funding from Peterhouse, S.H. and C.D. from the Royal Society. F.C.-S. acknowledges CONACYT Mexico. Correspondence and requests for materials should be addressed to S.H. Supplementary Information accompanies this paper on www.nature.com/naturematerials.

Reprints and permission information is available online at <http://npg.nature.com/reprintsandpermissions/>